

MOX-Report No. 48/2020

**Anisotropic adapted meshes for image segmentation:
application to 3D medical data**

Clerici, F.; Ferro, N.; Marconi, S.; Micheletti, S.; Negrello, E.;
Perotto, S.

MOX, Dipartimento di Matematica
Politecnico di Milano, Via Bonardi 9 - 20133 Milano (Italy)

mox-dmat@polimi.it

<http://mox.polimi.it>

Anisotropic adapted meshes for image segmentation: application to 3D medical data

Francesco Clerici[†], Nicola Ferro[#], Stefania Marconi[‡], Stefano Micheletti[#],
Erika Negrello[◇], Simona Perotto[#]

June 26, 2020

[†] INRIA Saclay Ile-de-France, 1, rue Honoré d'Estienne d'Orves
91126 Palaiseau, France, francesco.clerici@inria.fr

[#] MOX – Modellistica e Calcolo Scientifico, Dipartimento di Matematica
Politecnico di Milano, Piazza L. da Vinci 32, I-20133 Milano, Italy
{[nicola.ferro](mailto:nicola.ferro@polimi.it),[stefano.micheletti](mailto:stefano.micheletti@polimi.it),[simona.perotto](mailto:simona.perotto@polimi.it)}@polimi.it

[‡] Dipartimento di Ingegneria Civile e Architettura, Università di Pavia
Via Ferrata, 3, I-27100 Pavia, Italy, stefania.marconi@unipv.it

[◇] Fondazione IRCCS Policlinico San Matteo, Viale Golgi, 19, I-27100 Pavia, Italy
erika.negrello01@universitadipavia.it

Abstract

This work focuses on a variational approach to image segmentation based on the Ambrosio-Tortorelli functional. We propose an efficient algorithm, which combines the functional minimization with a smart choice of the computational mesh. With this aim, we resort to an anisotropic mesh adaptation procedure driven by an a posteriori recovery-based error analysis. We apply the proposed algorithm to a Computed Tomography dataset of a fractured pelvis, to create a virtual model of the anatomy. The result is verified against a semi-automatic segmentation carried out using the ITK-SNAP tool. Furthermore, a physical replica of the virtual model is produced by means of Fused Filament Fabrication technology, to assess the appropriateness of the proposed solution in terms of resolution-quality balance for 3D printing production.

Keywords: image segmentation, variational model, anisotropic mesh adaptation, a posteriori error estimator, additive manufacturing

AMS: 65N30, 65N50, 65K10, 68U10

1 Introduction

Image segmentation is the process of partitioning a digital image into multiple sets of pixels in order to obtain a simplified representation, more meaningful and easier to

analyze. This is reached by assigning a label to every pixel such that tiles with the same label share certain characteristics (e.g., color, intensity, texture) [38]. For instance, in the medical field, automated delineation of different image components is used for analyzing anatomical structures and tissue types, spatial distribution of function and activity, pathological regions. Applications can be various, as tumor edge identification, evaluation of fractures, surgical access definition, location of a stent deployment site, starting from the elaboration of volumetric radiologic image dataset (e.g., Multi-Detector Computed Tomography (MDCT), Magnetic Resonance (MR)).

The result of an image segmentation process applied to a 3D dataset can be transformed into a 3D virtual anatomical model, by means of rendering tools, and then possibly into a physical replica by means of Additive Manufacturing (AM) techniques. Both virtual and physical models enable the exploration of the target anatomy by clinicians, thus supporting the diagnosis and the planning process of complex interventional management, for intra-operative navigation and for surgical training purposes [39]. In particular, AM is gaining popularity in many fields, including healthcare, thanks to the capability to reproduce complex geometries, such as solid organs or major blood vessels [37]. Moreover, the creation of a patient-specific anatomical model is instrumental to the personalization of the treatment, one of the keys of modern precision medicine.

AM technologies include a wide range of different solutions, which are all based on the same approach: the selected object is manufactured through a layer-by-layer process. Various technologies differ in the way layers are deposited, according to the type of material employed. Through the so-called “slicing” process, the 3D virtual model is converted into a series of 2D slices and then into a set of instructions to drive the 3D printer operations for each layer. Among the various technologies, Fused Deposition Modeling (FDM - trademarked by Stratasys) or Fused Filament Fabrication (FFF - the open source equivalent term) machines are the most widespread on the market, since they have a wide range of prizes, including also few hundreds euro solutions and affordable printing materials. In FFF printers, a thermoplastic filament is pushed through a heating chamber, extruded through a small nozzle and deployed layer by layer, following the designated path.

The slicing process starts from the virtual model of the geometry, commonly provided in Standard Triangulation Language (STL) format. The more the geometry is detailed in terms of number of triangles, the more the slicing process will take, sometimes failing due to the overwhelming computational burden. To contain this issue, many slicing programs subsample the virtual geometry before the 3D printing, but this is particularly critical when dealing with anatomical models, for which the loss of details can impair the clinical evaluation.

Virtual models of patient-specific anatomies can be used to perform computational simulations as well. In this context, the smart choice of the computational mesh represents a crucial issue, being required to ensure a good compromise between simulation accuracy and computational effort. Mesh adaptation provides a possible solution to strike this balance. In particular, anisotropic adapted meshes proved to be very effective since they allow a very fine control of the geometric features of the elements (size, shape

and orientation) by aligning the shortest element size to the direction of the gradient of the physical variable of interest [7, 16, 17, 43, 44, 45, 46, 47, 48, 49, 50, 51, 52, 53]. As far as a segmentation problem is concerned, the gradient of the image intensity is usually tracked.

Goal of the present work is to enrich a variational approach to image segmentation based on the minimization of the Ambrosio-Tortorelli functional [4, 5] with an anisotropic mesh adaptation procedure. We extend [8] to the more challenging case of a 3D segmentation, by devising the new algorithm MES AMIS (MESH adaptation with Alternating Minimization for Image Segmentation). This algorithm is applied to a MDCT dataset of a fractured pelvis, with the aim of creating a virtual model of the anatomy, verified against a semi-automatic segmentation carried out in ITK-SNAP [11]. Furthermore, an experimental validation is performed by producing a physical replica of the virtual model by means of a FFF technology. The MES AMIS procedure proved to be effective for the reconstruction and 3D printing of the anatomical district of interest, thanks to a significant reduction of the amount of data to be processed during the slicing phase. The comparison with a state-of-the-art software together with this experimental validation represent a remarkable improvement over the pure numerical 2D context in [8].

The paper is organized as follows. Section 2 introduces the variational model based on the Ambrosio-Tortorelli functional together with the alternating minimization fixed point method used to deal with the non-convexity of the functional. In section 3, we provide the anisotropic setting and the mathematical tool employed to drive the mesh adaptation. We devise the MES AMIS algorithm in section 4, which is successively numerically verified against ITK-SNAP in section 5 and experimentally validated in section 6 by 3D printing a physical replica of the virtual model. Some conclusions and perspectives are finally drawn in section 7.

2 The discretized Ambrosio-Tortorelli functional

Among image segmentation algorithms, the class of the level set methods [9, 10] and the variational models [4, 5, 59] have been extensively studied and employed in practice. These methods become even more effective when coupled with mesh adaptation procedures [8, 58, 19, 12]. The segmentation method that we propose is based on a variational approach, where the image is idealized as a function f defined over $\Omega \subset \mathbb{R}^3$ taking values in $[0, 255]$. A suitable functional, which consists of a fidelity contribution to the original image plus extra-regularization terms, is minimized. One of the most well-known choice in this class is represented by the Mumford-Shah functional [2]

$$I(u, E) = \int_{\Omega} (u - f)^2 d\Omega + \beta \int_{\Omega \setminus E} |\nabla u|^2 d\Omega + \gamma \mathcal{H}^2(E), \quad (1)$$

where β and γ are positive constants to be tuned, the image $f \in L^\infty(\Omega)$, $E \subset \Omega$ is a closed set defining the separating edge, and \mathcal{H}^2 denotes the 2-dimensional Hausdorff measure. Functional $I(u, E)$ is minimized over $u \in C^1(\Omega \setminus E)$ and the set E . The first term of (1) represents the fidelity of the approximated image, u , to the original one.

The second term provides a control over the gradient of the approximated image outside the objects borders, while the last term controls the total area of the objects to be segmented.

It has been proved that the minimization problem admits at least one solution [3], and the set E is at most a countably union of surfaces of class C^1 . This problem is hard to be handled numerically, because of the presence of the 2-dimensional entity, E , embedded in a 3D Euclidean space.

In order to avoid to deal with lower dimensional entities, it is customary to solve an approximate version of (1). The driving idea is to substitute the argument E in $I(u, E)$ with an indicator-like function, v , suitably smoothed. An example of such a procedure has been proposed by L. Ambrosio and V.M. Tortorelli [4], given by

$$I_\epsilon(u, v) = \int_{\Omega} (u - f)^2 d\Omega + \beta \int_{\Omega} (v^2 + \eta) |\nabla u|^2 d\Omega + \gamma \int_{\Omega} \left(\epsilon |\nabla v|^2 + \frac{1}{4\epsilon} (v - 1)^2 \right) d\Omega, \quad (2)$$

where the minimum is searched in the space $V = H^1(\Omega) \times (H^1(\Omega) \cap L^\infty(\Omega))$, $\epsilon > 0$ and $\eta = O(\epsilon^2)$ is a positive parameter. Function v takes values in $[0, 1]$ and provides an approximate indicator of the set E , with thickness ϵ . The second term forces v to get close to zero in the neighborhood of an object boundary, where a sharp variation of the image occurs, whereas the last integral makes v to be close to 1 far from the boundaries. It is shown that the functional in (2) Γ -converges to the Mumford-Shah functional as $\epsilon \rightarrow 0$, in the strong topology of $L^2(\Omega)$ [5].

The functional (2) is not jointly convex because of the term $v^2 |\nabla u|^2$, and the existence of a minimum is not guaranteed. Functional I_ϵ is convex in u and v separately, so that a suitable alternating optimization procedure will be employed in the sequel [54]. For this purpose, the Gâteaux derivatives of the functional I_ϵ with respect to u and v along the directions ϕ and ψ , respectively, are computed as

$$\begin{aligned} I_{\epsilon,u}(u, v)\phi &= 2 \int_{\Omega} (u - f)\phi d\Omega + 2\beta \int_{\Omega} (v^2 + \eta) \nabla u \cdot \nabla \phi d\Omega =: 2a(v; u, \phi), \\ I_{\epsilon,v}(u, v)\psi &= 2\beta \int_{\Omega} |\nabla u|^2 v \psi d\Omega + \frac{\gamma}{2\epsilon} \int_{\Omega} (v - 1)\psi d\Omega + 2\gamma\epsilon \int_{\Omega} \nabla v \cdot \nabla \psi d\Omega =: 2b(u; v, \psi). \end{aligned}$$

Hence, the minimizers of I_ϵ satisfy

$$I'_\epsilon(u, v; \phi, \psi) := 2(a(v; u, \phi) + b(u; v, \psi)) = 0 \quad (3)$$

for all $(\phi, \psi) \in V$. It can be proved that the function v enjoys the following

Proposition 2.1 *If $(u, v) \in V$ is a critical point of I_ϵ , then $0 \leq v \leq 1$ a.e. in Ω .*

This proposition supports the interpretation of v as a smoothed indicator of the boundaries of the image f , and it can be proved by contradiction using a truncation argument [6]. We discretize the functional (2) in the context of the finite element method [55]. Let $\{\mathcal{T}_h\}_{h>0}$ be a family of conforming tetrahedral meshes of a domain Ω and let V_h be the associated space of continuous piecewise affine finite elements

$$V_h = \{v \in C^0(\overline{\Omega}) : v|_K \in \mathbb{P}_1, \forall K \in \mathcal{T}_h\}.$$

Now, we introduce the discrete counterpart of I_ϵ given by

$$\begin{aligned}
I_{\epsilon,h}(u_h, v_h) &= \int_{\Omega} P_h((u_h - f_h)^2) d\Omega + \beta \int_{\Omega} (P_h(v_h^2) + \eta) |\nabla u_h|^2 d\Omega \\
&+ \gamma \int_{\Omega} \left(\epsilon |\nabla v_h|^2 + \frac{1}{4\epsilon} P_h((v_h - 1)^2) \right) d\Omega,
\end{aligned} \tag{4}$$

where $(u_h, v_h) \in V_h^2$, $f_h \in V_h$ is a suitable approximation of f , and $P_h : C^0(\bar{\Omega}) \rightarrow V_h$ is the Lagrangian interpolant on V_h [55]. The Gâteaux derivatives of $I_{\epsilon,h}$ are

$$\begin{aligned}
I_{\epsilon,u,h}(u_h, v_h; \phi_h) &= 2 \int_{\Omega} P_h((u_h - f_h)\phi_h) d\Omega + 2\beta \int_{\Omega} (P_h(v_h^2) + \eta) \nabla u_h \cdot \nabla \phi_h d\Omega \\
&=: 2a_h(v_h; u_h, \phi_h), \\
I_{\epsilon,v,h}(u_h, v_h; \psi_h) &= 2\beta \int_{\Omega} |\nabla u_h|^2 P_h(v_h \psi_h) d\Omega + \frac{\gamma}{2\epsilon} \int_{\Omega} P_h((v_h - 1)\psi_h) d\Omega \\
&+ 2\gamma\epsilon \int_{\Omega} \nabla v_h \cdot \nabla \psi_h d\Omega =: 2b_h(u_h; v_h, \psi_h),
\end{aligned} \tag{5}$$

for every pair $(\phi_h, \psi_h) \in V_h^2$. The operator P_h allows us to guarantee the discrete analogue of Proposition 2.1 [6, 7]. Functional (4) is not jointly convex in u_h and v_h , analogously to its continuous counterpart. This justifies the employment of the alternating optimization procedure shown in Algorithm 1.

Algorithm 1 AMIS: Alternating Minimization for Image Segmentation

```

1: function AMIS( $f, \epsilon, \eta, \beta, \gamma, v_0, \text{F xv}, \text{J max}$ )
2:   Set  $\text{Ev h} = 1 + \text{F xv}$ ;
3:   Set  $v_h^{(0)} = v_0$ ;
4:   Set  $f_h = \mathcal{Q}_h f$ ;
5:   Set  $j = 0$ ;
6:   while  $\text{Ev h} > \text{F xv}$  &  $j < \text{J max}$  do
7:      $u_h^{(j)} = \arg \min_{z_h \in V_h} I_{\epsilon,h}(z_h, v_h^{(j)})$ ;
8:      $v_h^{(j+1)} = \arg \min_{z_h \in V_h} I_{\epsilon,h}(u_h^{(j)}, z_h)$ ;
9:      $\text{Ev h} = \|v_h^{(j+1)} - v_h^{(j)}\|_{L^\infty(\Omega)}$ ;
10:     $j = j + 1$ ;
11:  return  $u_h^{(j-1)}, v_h^{(j)}$ 

```

AMIS algorithm receives as input the image, f , the parameters $\epsilon, \eta, \beta, \gamma$ in (4), the initial guess, v_0 , for the approximate indicator, the tolerance F xv and the maximum number, J max , for the fixed point iterations associated with the alternating minimization. The operator \mathcal{Q}_h in line 4 is the $L^2(\Omega)$ -projection onto the space V_h and it turns the pixel image into a finite element function.

3 Anisotropic a posteriori error analysis

Mesh adaptation has been combined with the minimization of the Ambrosio-Tortorelli functional in the context of crack propagation in brittle materials (see, e.g., [7, 56, 57, 45, 6]), and of segmentation of 2D images [8, 19]. These previous works can be classified according to the type of mesh adaptation, by distinguishing between isotropic and anisotropic grids. We decide upon adopting an anisotropic framework, backed up by the consolidated computational superiority of anisotropic over isotropic meshes [7, 16, 17, 43, 44, 45, 46, 47, 48, 49, 50, 51, 52, 53]. We first introduce the anisotropic quantities describing a tetrahedral conforming mesh. Following [17, 46, 15, 16], we consider the affine map, $T_K : \hat{K} \rightarrow K$, which characterizes a mesh element $K \in \mathcal{T}_h$, starting from the reference tetrahedron \hat{K} , inscribed in the unit sphere with a vertex at $(0, 0, 1)$, such that

$$\mathbf{x} = T_K(\hat{\mathbf{x}}) = M_K \hat{\mathbf{x}} + \mathbf{t}_K,$$

where $M_K \in \mathbb{R}^{3 \times 3}$ is the Jacobian of T_K , and $\mathbf{t}_K \in \mathbb{R}^3$ denotes a shift vector. Combining the polar decomposition of M_K , $M_K = B_K Z_K$, with the spectral decomposition of B_K , we have

$$M_K = R_K^T \Lambda_K R_K Z_K,$$

where B_K is a symmetric and positive definite matrix, and Z_K is an orthogonal matrix. In particular, B_K acts on the reference tetrahedron as a stretch, while Z_K applies a rotation. The diagonal matrix Λ_K collects the eigenvalues of B_K , and R_K^T gathers by columns the corresponding eigenvectors, namely

$$\Lambda_K = \text{diag}(\lambda_{1,K}, \lambda_{2,K}, \lambda_{3,K}), \quad R_K^T = [\mathbf{r}_{1,K}, \mathbf{r}_{2,K}, \mathbf{r}_{3,K}],$$

with $\lambda_{1,K} \geq \lambda_{2,K} \geq \lambda_{3,K} > 0$. The eigenvectors describe the directions of the semi-axes of the ellipsoid circumscribing the element K , while the eigenvalues measure their length (see Figure 1). The deformation of tetrahedron K is quantified by the three aspect ratios

$$s_{1,K} = \left(\frac{\lambda_{1,K}^2}{\lambda_{2,K} \lambda_{3,K}} \right)^{2/3}, \quad s_{2,K} = \left(\frac{\lambda_{2,K}^2}{\lambda_{1,K} \lambda_{3,K}} \right)^{2/3}, \quad s_{3,K} = \left(\frac{\lambda_{3,K}^2}{\lambda_{1,K} \lambda_{2,K}} \right)^{2/3}, \quad (6)$$

such that $s_{1,K} \geq s_{2,K} \geq s_{3,K}$ and $s_{1,K} s_{2,K} s_{3,K} = 1$ [15, 16].

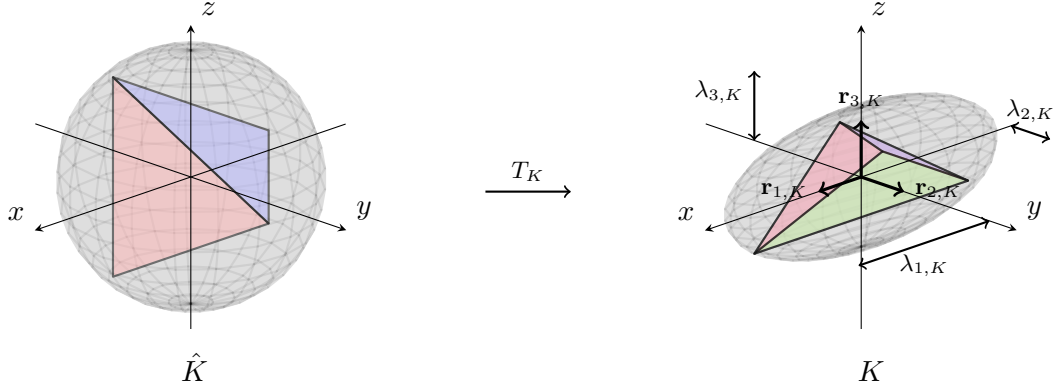


Figure 1: Action of the affine map T_K on the reference tetrahedron.

The next proposition provides the theoretical result supporting the anisotropic mesh adaptation procedure.

Proposition 3.1 *Let $(u_h, v_h) \in V_h^2$ be a critical point of $I_{\epsilon, h}$. If the cardinality $\#\Delta_K < \mathcal{N}$, for some $\mathcal{N} \in \mathbb{N}^+$, and if $\text{diam}(T_K^{-1}(\Delta_K)) < \mathcal{D}$, where $\Delta_K = \{T \in \mathcal{T}_h : T \cap K \neq \emptyset\}$, uniformly with respect to $K \in \mathcal{T}_h$, then it holds*

$$|I'_\epsilon(u_h, v_h; \phi, \psi)| \leq C \sum_{K \in \mathcal{T}_h} \{\rho_K^A(u_h, v_h) \omega_K(\phi) + \rho_K^B(u_h, v_h) \omega_K(\psi)\} \quad (7)$$

for any $(\phi, \psi) \in H^1(\Omega) \times (H^1(\Omega) \cap L^\infty(\Omega))$, where $I'_\epsilon(\cdot, \cdot; \cdot, \cdot)$ is defined as in (3), C is a positive constant depending on \mathcal{N} and \mathcal{D} , while

$$\begin{aligned} \rho_K^A(u_h, v_h) &= \|u_h - f\|_{L^2(K)} + 2\beta \|v_h(\nabla v_h \cdot \nabla u_h)\|_{L^2(K)} \\ &\quad + \frac{\beta}{2} \|[\nabla u_h]\|_{L^\infty(\partial K)} \|v_h^2 + \eta\|_{L^2(\partial K)} \left(\frac{h_K}{\lambda_{1,K} \lambda_{2,K} \lambda_{3,K}} \right)^{\frac{1}{2}} \\ &\quad + \frac{1}{\lambda_{3,K}} \|v_h^2 - P_h(v_h^2)\|_{L^\infty(K)} \|\nabla u_h\|_{L^2(K)} + \frac{h_K^2}{\lambda_{3,K}} |u_h - f_h|_{W^{1,\infty}(K)}, \end{aligned}$$

$$\begin{aligned} \rho_K^B(u_h, v_h) &= \left\| \left(\beta |\nabla u_h|^2 + \frac{\gamma}{4\epsilon} \right) v_h - \frac{\gamma}{4\epsilon} \right\|_{L^2(K)} + \frac{\gamma\epsilon}{2} \|[\nabla v_h]\|_{L^2(\partial K)} \left(\frac{h_K}{\lambda_{1,K} \lambda_{2,K} \lambda_{3,K}} \right)^{\frac{1}{2}} \\ &\quad + \frac{h_K^2}{\lambda_{3,K}} \left\| \beta |\nabla u_h|^2 + \frac{\gamma}{4\epsilon} \right\|_{L^2(K)} |v_h|_{W^{1,\infty}(K)}, \end{aligned}$$

$$\omega_K(z) = \left[\sum_{i=1}^3 \lambda_{i,K}^2 (\mathbf{r}_{i,K}^T G_{\Delta_K}(z) \mathbf{r}_{i,K}) \right]^{\frac{1}{2}} \quad \forall z \in H^1(\Omega), \quad (8)$$

where h_K is the diameter of the tetrahedron K , and

$$[[\nabla w_h]] = \begin{cases} |[\nabla w_h \cdot \mathbf{n}]| & \text{on } \mathcal{E}_h \\ |[\nabla w_h \cdot \mathbf{n}]| & \text{on } \mathcal{E}_h \cap \partial\Omega, \end{cases}$$

is the absolute value of the jump of the normal derivative, with \mathbf{n} the unit normal vector to the generic element face in the skeleton \mathcal{E}_h of \mathcal{T}_h . The symmetric positive semidefinite matrix $G_{\Delta_K}(z)$ is defined by

$$[G_{\Delta_K}(z)]_{ij} = \int_{\Delta_K} \frac{\partial z}{\partial x_i} \frac{\partial z}{\partial x_j} d\mathbf{x} \quad \text{with } i, j = 1, 2, 3. \quad (9)$$

Proof: The proof of this result can be obtained by merging the analysis in [8] and by exploiting the property of the operator \mathcal{Q}_h . \square

The estimate (7) holds for any pair $(\phi, \psi) \in H^1(\Omega) \times (H^1(\Omega) \times L^\infty(\Omega))$. Following [7, 8], we choose $\phi = u - u_h$ and $\psi = v - v_h$, so that the term $I'_\epsilon(u_h, v_h; \phi, \psi)$ becomes proportional to the functional error $I_\epsilon(u, v) - I_\epsilon(u_h, v_h)$, up to a third-order remainder term. Finally, in order to make the right-hand side in (7) explicitly computable, we replace the weights $\omega_K(u - u_h)$ and $\omega_K(v - v_h)$ in (8) with

$$\omega_K^R(z_h) = \left[\sum_{i=1}^3 \lambda_{i,K}^2 (\mathbf{r}_{i,K}^T G_{\Delta_K}^R(z_h) \mathbf{r}_{i,K}) \right]^{\frac{1}{2}}, \quad \text{with } z_h = u_h, v_h,$$

where $G_{\Delta_K}^R(z_h)$ is the matrix with entries

$$[G_{\Delta_K}^R(z_h)]_{ij} = \int_{\Delta_K} \left(\mathcal{R}_i(z_h) - \frac{\partial z_h}{\partial x_i} \right) \left(\mathcal{R}_j(z_h) - \frac{\partial z_h}{\partial x_j} \right) d\mathbf{x} \quad \text{with } i, j = 1, 2, 3,$$

with $\mathcal{R}(z_h) = [\mathcal{R}_1(z_h), \mathcal{R}_2(z_h), \mathcal{R}_3(z_h)]^T$ the Zienkiewicz-Zhu recovered gradient of z_h [13, 14]. In particular, we have adopted the volume-weighted average in [15, 16]

$$\mathcal{R}(z_h)(\mathbf{x}) = \frac{1}{|\Delta_K|} \sum_{T \in \Delta_K} |T| \nabla z_h|_T \quad \forall \mathbf{x} \in \Delta_K.$$

To sum up, the actual anisotropic error estimator is provided by $\zeta = \sum_{K \in \mathcal{T}_h} \zeta_K$, where

$$\zeta_K = \rho_K^A(u_h, v_h) \omega_K^R(u_h) + \rho_K^B(u_h, v_h) \omega_K^R(v_h). \quad (10)$$

We now exploit the estimator ζ to set up the anisotropic mesh adaptation procedure. For this purpose, we adopt a metric-based approach, following [18]. The adapted mesh is induced by a metric, i.e., a positive definite tensor field, \widetilde{M}_N , associated with the nodes of the current mesh. The challenge is to convert estimator ζ into \widetilde{M}_N . Following [15, 16], we first derive a piecewise constant metric, \widetilde{M} , such that $\widetilde{M}|_K = \widetilde{M}_K = \sum_{i=1}^3 \widetilde{\lambda}_{i,K}^{-2} \widetilde{\mathbf{r}}_{i,K} \widetilde{\mathbf{r}}_{i,K}^T$, which ensures a certain accuracy, τ , on ζ , while minimizing the cardinality of the mesh and equidistributing the error estimator throughout the elements. The outcome of this procedure is stated in the following result.

Proposition 3.2 *Let τ be the tolerance demanded by the user on ζ . Then, the local metric \widetilde{M}_K equidistributing the error and minimizing the number of elements is provided by*

$$\widetilde{\lambda}_{i,K} = \left(\frac{\tau}{\sqrt{3}|\widehat{K}|\#\mathcal{T}_h} \right)^{\frac{1}{4}} \left(\prod_{i=1}^3 g_{i,K} \right)^{\frac{1}{8}} g_{4-i,K}^{-\frac{1}{2}},$$

and

$$\mathbf{r}_{i,K} = \mathbf{g}_{4-i,K},$$

for $i = 1, 2, 3$, where $\{g_{i,K}, \mathbf{g}_{i,K}\}$ are the eigenpairs of the matrix

$$\Gamma_K = (\bar{\rho}_K^A(u_h, v_h))^2 \overline{G}_{\Delta_K}^R(u_h) + (\bar{\rho}_K^B(u_h, v_h))^2 \overline{G}_{\Delta_K}^R(v_h),$$

where the quantities

$$\bar{\rho}_K^Z(u_h, v_h) = \frac{\rho_K^Z(u_h, v_h)}{\left[|\widehat{K}| \prod_{i=1}^3 \lambda_{i,K} \right]^{\frac{1}{2}}}, \quad \overline{G}_{\Delta_K}^R(z_h) = \frac{G_{\Delta_K}^R(z_h)}{|\widehat{K}| \prod_{i=1}^3 \lambda_{i,K}},$$

with $Z = A, B$ and $z_h = u_h, v_h$, have been scaled to the volume of K , $|K| = |\widehat{K}| \prod_{i=1}^3 \lambda_{i,K}$.

Then, the nodewise metric \widetilde{M}_N is computed via a volume-weighted average over the patch, Δ_N , of the elements sharing the node N , namely,

$$\widetilde{M}_N = \frac{3}{8} \frac{1}{|\Delta_N|} \sum_{K \in \Delta_N} |K| \widetilde{M}_K,$$

where the factor $\frac{3}{8}$ shrinks the reference tetrahedron to a unit edge one. This is justified by the property that an optimal mesh is such that each edge has unit length with respect to the associated metric [18].

Remark 3.1 *In practice, it is advisable to check whether the predicted number of elements is computationally affordable, i.e., to within a maximum value $NMAX$. The expected number, $\#\widetilde{M}$, of tetrahedra associated with \widetilde{M} is*

$$\#\widetilde{M} = \sum_{K \in \mathcal{T}_h} 1 = \sum_{K \in \mathcal{T}_h} \int_K \frac{1}{|K|} dK = \sum_{K \in \mathcal{T}_h} \int_K \frac{1}{|\widehat{K}| \det(\widetilde{M}_K)^{-\frac{1}{2}}} dK, \quad (11)$$

which follows from the relations $\det(\widetilde{M}_K) = \prod_{i=1}^3 \widetilde{\lambda}_{i,K}^{-2}$, and $|K| = |\widehat{K}| \prod_{i=1}^3 \lambda_{i,K}$. This means that, when $\#\widetilde{M} > NMAX$, the metric is scaled so that

$$\widetilde{M}_K \leftarrow \left(\frac{NMAX}{\#\mathcal{T}_h} \right)^{\frac{2}{3}} \widetilde{M}_K. \quad (12)$$

This scaling preserves the shape and the orientation of K while modifying the element size only.

4 Anisotropic mesh adaptation for image segmentation

We now merge the segmentation procedure in section 2 with the mesh adaptation process in the previous section. For this purpose, following [8], we resort to an *optimize-then-adapt* strategy, as an alternative to an *optimize-and-adapt* procedure [6, 7, 56, 57].

The adopted procedure is named MES AMIS (MESH adaptation with Alternating Minimization for Image Segmentation) and it is listed in Algorithm 2. The input parameters to MES AMIS include the inputs to AMIS plus additional data, namely, the tolerances τ , TOLm, TOLi, TOLth, controlling the accuracy on the error estimator, the stagnation of the computational mesh throughout the adaptation procedure, the convergence of the energy functional in (4), and the threshold to extract the segmented surface, respectively, the maximum number NMAX of the allowed elements, the initial mesh, \mathcal{T}_h^0 , whose generation will be described in Section 5.

Algorithm 2 MES AMIS: MESH adaptation with Alternating Minimization for Image Segmentation

```

1: Input:  $f, \epsilon, \eta, \beta, \gamma, v_0, \text{F xv}, \text{Jmax}, \tau, \text{TOLm}, \text{TOLi}, \text{TOLth}, \text{NMAX}, \mathcal{T}_h^0$ 
2: Set  $\text{Em} = 1 + \text{TOLm}$ 
3: Set  $\text{Ei} = 1 + \text{TOLi}$ 
4: Set  $i = 0$ 
5: Set  $V_0 = v_0$ 
6: Set  $I_{old} = -1$ 
7: while  $\text{Em} > \text{TOLm}$  &  $\text{Ei} > \text{TOLi}$  do
8:    $[u_h^{(i)}, v_h^{(i)}] = \text{AMIS}(f, \epsilon, \eta, \beta, \gamma, V_0, \text{F xv}, \text{Jmax})$ 
9:    $\mathcal{T}_h^{(i+1)} = \text{adapt\_mesh}(u_h^{(i)}, v_h^{(i)}, \tau, \text{NMAX})$ 
10:  Set  $u_h^{(i+1)} = \Pi_{i \rightarrow i+1}(u_h^{(i)})$ ,  $v_h^{(i+1)} = \Pi_{i \rightarrow i+1}(v_h^{(i)})$ 
11:  Compute  $I_{new} = I_{\epsilon, h}(u_h^{(i+1)}, v_h^{(i+1)})$ 
12:   $\text{Em} = |\#\mathcal{T}_h^{(i+1)} - \#\mathcal{T}_h^{(i)}| / \#\mathcal{T}_h^{(i)}$ 
13:   $\text{Ei} = |I_{new} - I_{old}| / |I_{old}|$ 
14:   $I_{old} = I_{new}$ 
15:   $V_0 = v_h^{(i+1)}$ 
16:   $i = i + 1$ 
17: Set  $[\mathcal{T}_h^{th}, v_h^{th}] = \text{extract\_contours}(\mathcal{T}_h^{(i)}, v_h^{(i)}, \text{TOLth})$ 
18: Output:  $u_h^f = u_h^{(i)}, v_h^f = v_h^{(i)}, \mathcal{T}_h^f = \mathcal{T}_h^{(i)}, v_h^{th}, \mathcal{T}_h^{th}$ 

```

The convergence check involves both the stagnation of the mesh and of the functional (line 7) to control simultaneously the two phases of the *optimize-then-adapt* procedure. Function `adapt_mesh` construct the metric \widetilde{M} and generates the corresponding adapted mesh, $\mathcal{T}_h^{(i+1)}$. Before starting with a new iteration, functions u_h and v_h have to be interpolated on the new mesh for consistency, via the operator $\Pi_{i \rightarrow i+1}$. Function `extract_contours` performs a truncation of the mesh, so that $\mathcal{T}_h^{th} = \cup_{K \in \Theta} K$, with $\Theta = \{K \in \mathcal{T}_h : v_h(\mathbf{b}_K) < \text{TOLth}\}$, where \mathbf{b}_K is the centroid of the cell K , with associated

approximate indicator, $v_h^{th} = v_h|_{\mathcal{T}_h^{th}}$. The output quantities are the approximate image, u_h^f , and indicator, v_h^f , the final mesh, \mathcal{T}_h^f , the truncated approximate indicator, v_h^{th} , and grid, \mathcal{T}_h^{th} .

Algorithm MES AMIS has been implemented in FreeFEM [20], while mesh adaptation is carried out through the software suite Mmg PLATFORM [1]. Finally, starting from \mathcal{T}_h^{th} and v_h^{th} , the boundary surface mesh, Σ_h , is extracted using the open source software ParaView [22]. ParaView is also used to provide the visualization of the computational results in the next sections.

5 Numerical verification

The MES AMIS algorithm is applied to a MDCT (Multi Detector Computed Tomography) dataset of a fractured human pelvis.¹ This dataset contains the images of tissues of different nature: bone, soft tissues (as fat, muscles), cartilage and others. In a MDCT scan, the grayscale pixel intensity depends on the radiodensity of the tissue, which measures the associated opacity to radiomagnetic fields. In particular, low grayscale values identify air, fat, soft tissues and, in general, tissues with low radio-opacity, medium grayscale values correspond to fluids such as water, bile, or urine, while high grayscale values are associated with bones [21]. As a consequence, the segmentation of a fractured pelvis will be performed on a pre-processed image sequence, to manage the coexistence of tissues characterized by a different radiodensity. In particular, we apply a thresholding of the original image f by defining the thresholded image

$$f_t(\mathbf{x}) = \begin{cases} f(\mathbf{x}) & \text{if } f(\mathbf{x}) > 140 \\ 140 & \text{if } f(\mathbf{x}) \leq 140, \end{cases} \quad (13)$$

where the value 140 depends on the dataset at hand and is chosen so that the resulting image highlights the bone tissue, while removing the soft parts.

The region of interest consists of a set of 304 slices, which are uniformly stacked 1 mm apart. Each slice coincides with a $n_x \times n_y = 204 \times 244$ pixel image, and it is obtained by cutting out the original source characterized by a 512×512 pixel resolution. In Figure 2, we show the selected volumetric dataset reconstructed along the axial, sagittal and coronal planes. The three views are particularly helpful when evaluating the extent and morphology of the fracture.

To generate the initial mesh, \mathcal{T}_h^0 , we apply the following steps:

- i) we keep one out of two pixels along the x - and y -direction;
- ii) we associate each pixel with its centroid and we build a 3D structured parallelepiped grid with size $(n_x/2 - 1) \times (n_y/2 - 1) \times (n_z - 1)$, with n_z the number of stacked slices, whose vertices coincide with the pixel centroids;

¹Courtesy of Dipartimento di Radiologia, Fondazione IRCCS Policlinico San Matteo, Pavia, Italy. The case is retrospective, thus no image acquisition was carried out specifically for the present work. The image dataset includes the pelvic region and it is acquired at 1 mm of slice thickness without the use of contrast medium.



Figure 2: Visualization of the selected dataset along the axial (a), sagittal (b) and coronal (c) plane.

- iii) we subdivide each parallelepiped into six tetrahedra, by preserving the number of vertices.

The choice of reducing the dataset along the x - and y -direction is justified by memory allocation reasons related to the optimization routines in Algorithm AMIS. Mesh \mathcal{T}_h^0 is the one involved in the definition of the projection operator, \mathcal{Q}_h . As far as the image is concerned, f is first thresholded on each slice, and then associated with the vertices of the tetrahedra mesh.

Now we run the MES AMIS algorithm with the following input parameters: $f = f_t$, $\epsilon = 10^{-3}$, $\eta = \epsilon^2$, $\beta = 2.0$, $\gamma = 0.1$, $v_0 = 1$, $\text{Fvx} = 10^{-2}$, $\text{Jmax} = 10$, $\tau = 10^{-2}$, $\text{TOLm} = 10^{-2}$, $\text{TOLi} = 10^{-2}$, $\text{TOLth} = 10^{-1}$, $\text{NMAX} = 1.3 \times 10^6$, \mathcal{T}_h^0 being the mesh constructed as above. The tuning of the parameters characterizing functional I_ϵ is driven by the sensitivity analysis performed in [8] for the 2D case.

Algorithm 2 converges in 10 iterations, after 10779 seconds². Figure 3 shows the trend of the Ambrosio-Tortorelli functional (left) together with the evolution of the mesh cardinality (right). The two panels confirm the combined check performed in line 7 by MES AMIS algorithm.

In Figure 4 (a), we provide the surface thresholded by the algorithm. The cut-off value adopted in (13) leads to segment also the sacrum (see the two panels in Figure 5) and the femoral head besides the fractured hemipelvis. The final adapted mesh, \mathcal{T}_h^f , consists of $1.139 \cdot 10^6$ elements, while $1.148 \cdot 10^5$ triangles delimit the surface mesh, Σ_h , the maximum and average values of the three aspect ratios in (6), being $\max_{K \in \mathcal{T}_h^f} s_{1,K} = 101.52$, $\max_{K \in \mathcal{T}_h^f} s_{2,K} = 10.24$, $\max_{K \in \mathcal{T}_h^f} s_{3,K} = 0.92$, and $\bar{s}_{1,K} = 5.96$, $\bar{s}_{2,K} = 1.52$, $\bar{s}_{3,K} = 0.19$, respectively.

5.1 Comparison with ITK-SNAP

This investigation is carried out by comparing Algorithm 2 with the result of a semi-automatic segmentation performed by means of the open-source software ITK-SNAP [11]. ITK-SNAP is devoted to the segmentation of 3D medical images, which combines active contour methods [32] with manual delineation and image navigation. In more

²The processor used to perform the computation is an Intel Core i5-2310 @2.90GHz, and 8GB of RAM

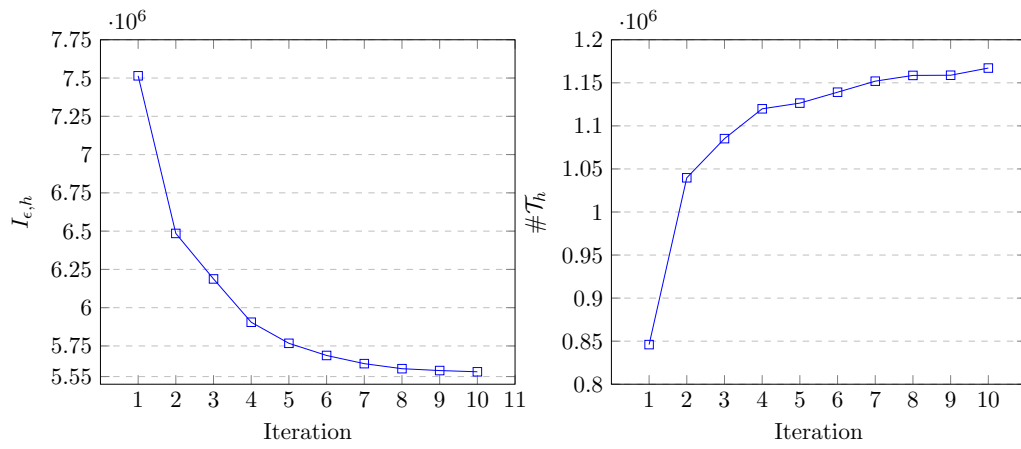
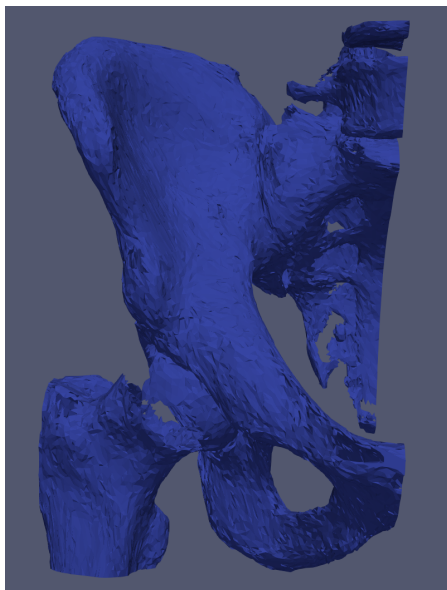
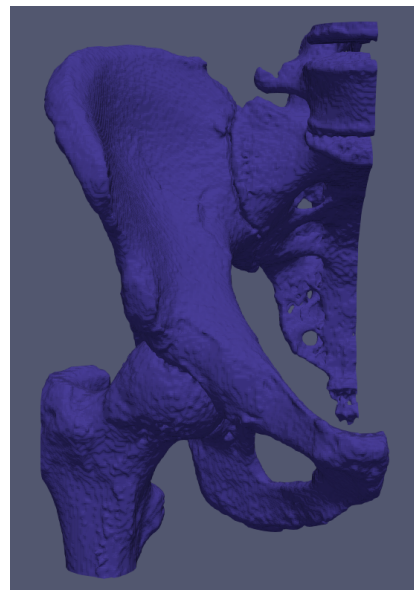


Figure 3: MES AMIS: convergence history of the functional $I_{\epsilon,h}$ (left) and of the cardinality of the mesh \mathcal{T}_h (right).



(a) MES AMIS



(b) ITK-SNAP

Figure 4: Comparison between MES AMIS and ITK-SNAP: reconstruction of a fractured hemipelvis.

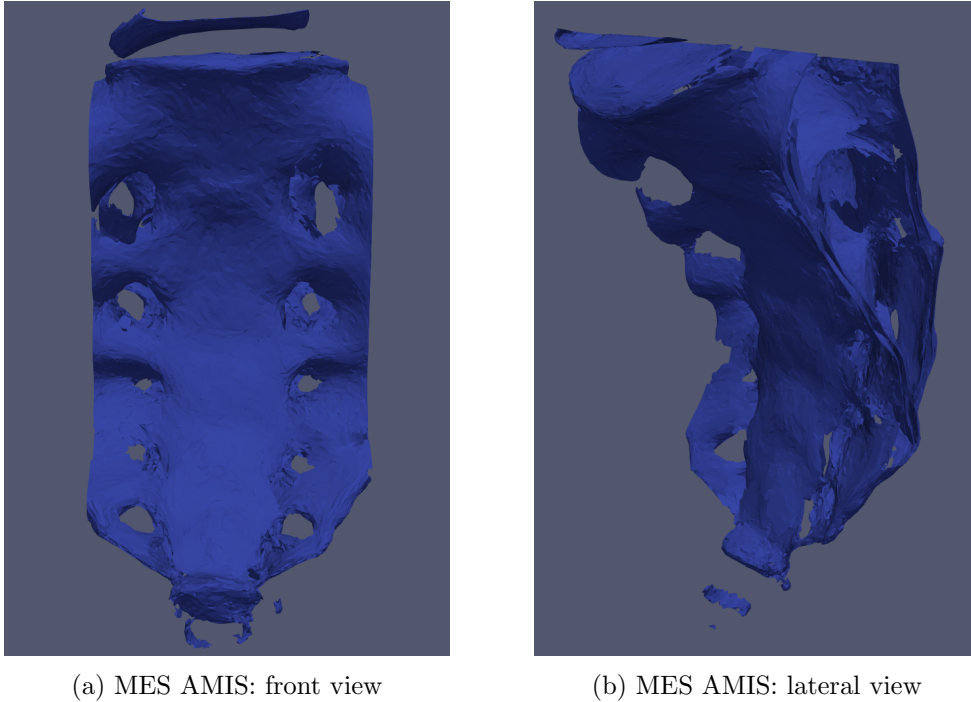


Figure 5: MES AMIS: reconstructed geometry of the sacrum.

detail, we have applied a geodesic active contour model on the original stack of 304 slices with a resolution of 204×244 pixels [23]. The choice of preserving the full dataset is justified on the one hand by the need of dealing with a high resolution surface as a reference model, on the other hand by the fact that ITK-SNAP can afford the storage and the processing of the whole data thanks to the employment of a narrow band formulation [24].

In particular, the surface reconstructed by MES AMIS is compared with a reference segmentation, Σ , called *ground truth*. This surface is obtained by means of a four-step semi-automatic procedure:

- a) Three experts³ are asked to perform a semi-automatic segmentation of the target structure using ITK-SNAP on the $n_x \times n_y \times n_z$ voxel grid;
- b) afterward, each expert is asked to manually correct the segmentation, still using ITK-SNAP, checking the consistency with the original structure. Thus, three independent label sets (“inside” or “outside” the segmented contour) are generated;
- c) a final labelling is obtained by a majority pronunciation (i.e., if a pixel is labelled in at least two out of three label sets, it is kept labelled also in the final set) based

³Biomedical engineers with at least three years of experience in processing and segmentation of medical images in the orthopedic field.

on these three inputs, and it is considered as a reference, and assumed perfectly coinciding with the real pelvis;

- d) starting from this labelling, a marching cube algorithm [42] provides the final triangulated *ground truth* surface Σ .

Alternative procedures to build the *ground truth* can be adopted, such as, a manual segmentation [27, 30, 29] or by resorting to mathematical techniques, which employ this manual segmentation as input data [28, 31].

Figure 4 (b) shows the *ground truth* yielded by ITK-SNAP, consisting of $1.389 \cdot 10^6$ triangles. The two panels in the figure are qualitatively comparable despite the large difference in the triangulation cardinality.

In the next two paragraphs, we investigate the robustness to the data resolution by considering all the 304 slices and only a subset of these.

Robustness to subsampling on the whole geometry We investigate the effect produced by a subsampling of the whole pelvis geometry with respect to the stack size in terms of quality of surface reconstruction. For this purpose, we carry out six numerical experiments where we run MES AMIS on an initial grid \mathcal{T}_h^0 obtained by replacing in item ii) n_z with n_z/s , with $s = 2i$ for $i = 1, \dots, 6$, while preserving the same values for all the other input parameters of Algorithm 2.

Table 1 collects the results of this investigation by providing the subsampling ratio, s , the cardinality of the final adapted mesh, \mathcal{T}_h^f , and of the surface triangulation, Σ_h . The variation of the two cardinalities in the table is essentially negligible, with a maximum discrepancy of 90.17% between Σ_h and Σ in terms of number of triangles. This can be ascribed to the constraint enforced through the input parameter NMAX in the algorithm MES AMIS.

In terms of computational effort, all the six runs require a CPU time between 9000 and 12600 seconds.

Table 1: Robustness of MES AMIS with respect to the subsampling on the whole geometry

s	$\#\mathcal{T}_h^f$	$\#\Sigma_h$
1	$1.139 \cdot 10^6$	$1.478 \cdot 10^5$
2	$1.136 \cdot 10^6$	$1.419 \cdot 10^5$
4	$1.129 \cdot 10^6$	$1.418 \cdot 10^5$
6	$1.109 \cdot 10^6$	$1.365 \cdot 10^5$
8	$1.120 \cdot 10^6$	$1.412 \cdot 10^5$
10	$1.108 \cdot 10^6$	$1.396 \cdot 10^5$
12	$1.119 \cdot 10^6$	$1.419 \cdot 10^5$

The accuracy of the seven segmentations in Table 1 is now quantified in terms of distance with respect to the *ground truth*. For this purpose, we adopt three distance

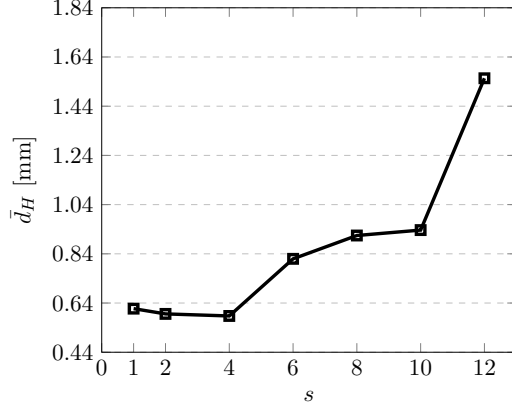


Figure 6: Comparison between MES AMIS and ITK-SNAP: average distance between the *ground truth* and Σ_h as a function of the subsampling level.

measures [25], namely the Hausdorff distance

$$d_H(\mathcal{S}'_h, \mathcal{S}''_h) = \max_{\mathbf{v} \in \mathcal{S}'_h} \min_{\mathbf{x} \in \mathcal{S}''_h} |\mathbf{v} - \mathbf{x}| \quad (14)$$

between the discrete surfaces, \mathcal{S}'_h and \mathcal{S}''_h , with \mathbf{v} the generic vertex of \mathcal{S}'_h and \mathbf{x} the generic point over \mathcal{S}''_h , $|\cdot|$ being the Euclidean norm; the average Hausdorff distance

$$\bar{d}_H(\mathcal{S}'_h, \mathcal{S}''_h) = \frac{1}{\#\mathcal{S}'_h} \sum_{\mathbf{v} \in \mathcal{S}'_h} \min_{\mathbf{x} \in \mathcal{S}''_h} |\mathbf{v} - \mathbf{x}|; \quad (15)$$

the local distance associated with the generic vertex $\mathbf{v} \in \mathcal{S}'_h$,

$$d_{loc}(\mathbf{v}) = \min_{\mathbf{x} \in \mathcal{S}''_h} |\mathbf{x} - \mathbf{v}|. \quad (16)$$

In particular, for comparison purposes, we identify \mathcal{S}'_h with the *ground truth*, \mathcal{S}''_h with Σ_h , and we resort to the CloudCompare [26] built-in functions to compute the distances.

Distance (15) makes the measure provided by (14) robuster with respect to the possible presence of outliers, which frequently characterizes a surface reconstruction procedure. Figure 6 shows the trend of the distance (15) as a function of the subsampling level, s , in Table 1.

In general, we expect a degradation of the values for \bar{d}_H as s increases, together with an unavoidable misalignment between the frames of reference associated with the two surfaces. This is confirmed in Figure 6, where the misalignment dominates in the range $1 \leq s \leq 4$, whereas the discrepancy between Σ and Σ_h overtakes the error due to misalignment for larger values of s . This allows us to discriminate among the subsamplings in Table 1, by inferring that the reconstructions associated with $s = 2, 4$ are the most effective since the error due to subsampling is on the same order of magnitude of the misalignment error.

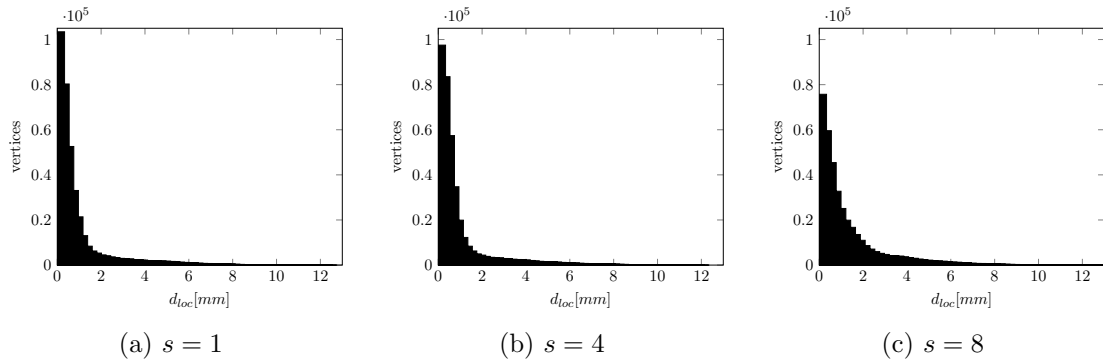


Figure 7: Comparison between MES AMIS and ITK-SNAP: histograms of d_{loc} for different values of s .

To complete this analysis, in Figure 7 we provide the histograms of the quantity in (16) for $s = 1, 4, 8$. We can appreciate an increase of the variance for larger values of s , with a corresponding deterioration of the segmentation.

Robustness to subsampling on a portion of the geometry We select a subregion of the whole hemipelvis coinciding with a small portion of the hip bone, which corresponds to the location of the largest fracture (see the area highlighted in Figure 8 (a)). In particular, we pick the volume emphasized in Figure 8 (b), consisting of a stack of 38 slices. This choice allows us a more thorough investigation, namely, first by preserving the original resolution along the x - and y -direction (204×244) and keeping all the 38 slices; then employing a 102×122 resolution per slice and carrying out the subsampling (along the z -direction) as in the previous paragraph.

For the sake of comparison, we need to build a new *ground truth*, which coincides with the surface in Figure 9 (b), comprising $1.132 \cdot 10^5$ triangles, obtained by running the four-step semi-automatic procedure described at the beginning of this section on the $204 \times 244 \times 38$ dataset. We observe that the surface shows a considerable level of roughness despite the large number of elements.

The MES AMIS algorithm is run on the selected subregion, by keeping the same values of all the input parameters as in the previous paragraph, except for $NMAX$, which is set to $2 \cdot 10^5$. Moreover, the initial mesh, \mathcal{T}_h^0 , is built by keeping all the pixels along the x - and y -direction, generating a 3D structured parallelepiped grid with size $203 \times 243 \times 37$ and subdividing each parallelepiped into six tetrahedra. The employment of a portion of the fractured hemipelvis allows us to perform a comparison between ITK-SNAP and MES AMIS at the full (and the same) resolution.

The algorithm stops after 10 iterations, by delivering the surface in Figure 9 (a), composed by $1.775 \cdot 10^4$ triangles. We observe a higher smoothness of this surface, when compared with the one in panel (b), despite one order of magnitude less elements.

The comparison between MES AMIS and ITK-SNAP is carried out in terms of the distances defined in (14)-(16). In particular, $d_H = 7.058$, $\bar{d}_H = 0.555$ and $\min d_{loc} = 0.0$.

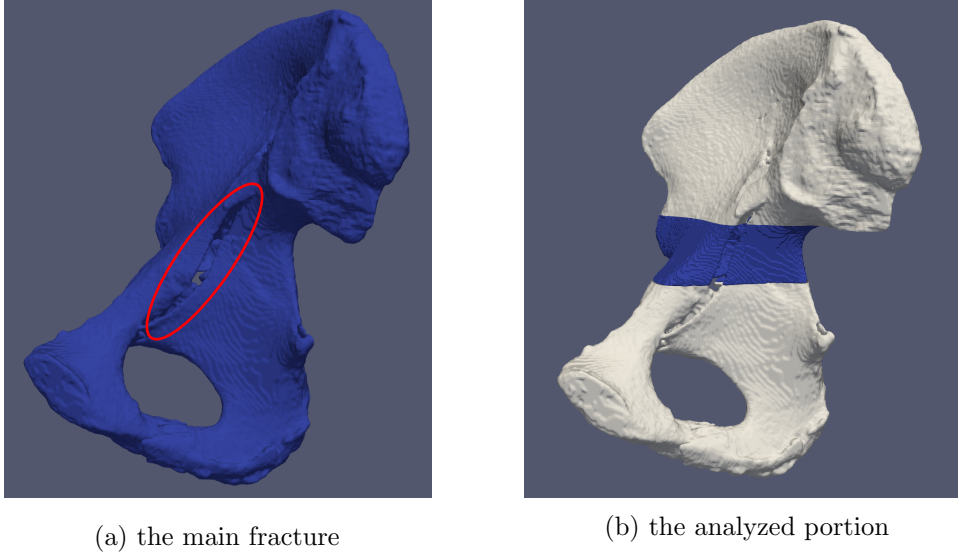


Figure 8: Comparison between MES AMIS and ITK-SNAP: partial subsampling check.

In Figure 10, we provide the distribution of d_{loc} over the vertices of the *ground truth*, obtained using CloudCompare [26]. We note that the larger mismatch is located in the regions inside the bone, since here the tissue is spongy and exhibits a high variability. This also depends strongly on the thresholding phase, in particular on the cut-off value used in (13). For these reasons, d_H is likely an overestimation of the actual distance.

To perform the subsampling along the z -direction, we halve again the resolution of each slice (102×122) and we consider $38/s$ slices, with $s = 1, 2, 4$, which amounts to considering 24.78%, 12.05% and 6.03% of the elements in \mathcal{T}_h^0 with respect to the cardinality of the initial mesh associated with the full resolution dataset. For each subsampling, we compute the average distance \bar{d}_H , which is provided in the second column of Table 2. The values of the distances are thoroughly comparable to each other and also to the distance associated with the full dataset, i.e., $\bar{d}_H^f = 0.555$. The last anomalous value (i.e., the minimum distance for the coarsest sampling) can be justified by the same sources of bias affecting the check on the full dataset. We also collect the percentage of the triangles in Σ_h with respect to the *ground truth* (third column), together with the distance variation percentage, computed as $(\bar{d}_H - \bar{d}_H^f)/\bar{d}_H^f$ (last column).

To sum up, the accuracy characterizing the segmentation provided by MES AMIS is thoroughly acceptable, with a contained value of the distance variation even though employing a small portion of the original dataset.

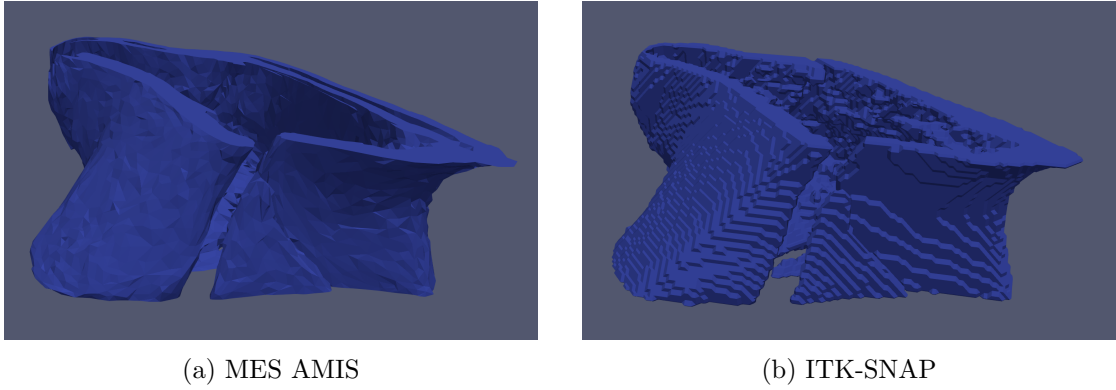


Figure 9: Comparison between MES AMIS and ITK-SNAP: reconstruction of a full-resolution portion of the fractured hip bone.

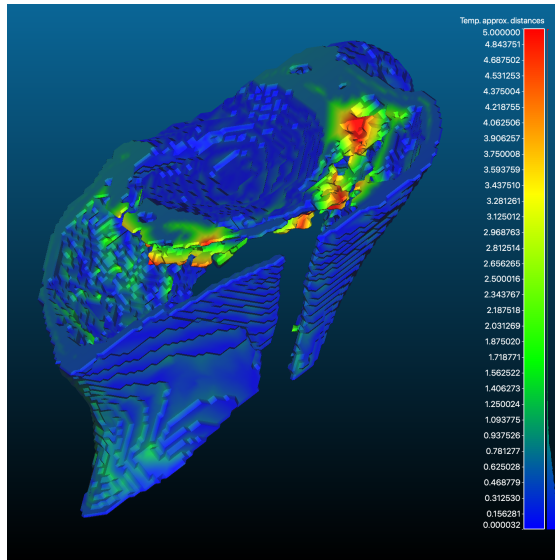


Figure 10: Comparison between MES AMIS and ITK-SNAP: distribution of d_{loc} over the ITK-SNAP surface.

Table 2: Comparison between MES AMIS and ITK-SNAP: subsampling on a portion of the whole geometry

s	\bar{d}_H [mm]	triangles reduction [%]	distance variation [%]
1	0.617	84.32	11.17
2	0.596	90.53	7.39
4	0.587	90.54	5.77

6 Experimental Validation: Additive Manufacturing testing

We test the effectiveness of the surface reconstruction provided by MES AMIS for the manufacturing of a physical replica using Additive Manufacturing (AM) technology. The assessment of the quality of a 3D printed model is not a trivial task in many cases. When the original physical object is available, the validation of the accuracy of 3D printed objects can be carried out by measuring the two objects with a caliper, or by comparing the scan of the 3D printed replica with the scan of the original object [33, 36, 34, 35]. In the medical field, it is almost impossible to directly measure the structure to be replicated. Moreover, even if the anatomical sample is available, it is very difficult to deal with a direct assessment.

In the present work, we rely on a qualitative approach, by assessing the presence and the level of detail of the most important features of interest for the surgical planning. The overall quality of the final 3D printed model depends on many factors, such as the resolution of the machine, the employed material, the specific set of printing parameters (e.g., extrusion temperature, speed, flow rate, deposition pattern), but also on the way the virtual model is processed by the software employed for the slicing phase. A standard input data to a slicing software is a discrete representation of the virtual geometry (i.e., the triangular mesh Σ_h), commonly stored in an STL (namely, Stereolithography or Standard Triangulation Language) file. Successively, the slicing software cuts the virtual geometry in a sequence of slices, with a thickness equal to the height of the corresponding layer to be deposited, according to the selected parameters. Then, each slice is processed so that the commands to deploy the material in each layer are issued, following the prescribed path. In particular, machine instructions provide a list of spatial coordinates to move the printing head and to control the speed and the amount of material to be extruded.

To manufacture the pelvis replica, we use a 3NTR A4v4 Fused Filament Fabrication (FFF) machine equipped with three extruders able to reach an extrusion temperature of $410^{\circ}C$, thus suitable also for high performance materials, a heated bed up to $120^{\circ}C$, and a heated chamber up to $80^{\circ}C$. Concerning the material, we employ Acrylonitrile Butadiene Styrene (ABS) for the model, and High Impact PolyStyrene (HIPS) for the support, being easy to mechanically detach from ABS, or soluble in limonene solution for the most complex cases.

Unlike other AM technologies, such as Binder Jetting or Material Jetting machines, the number of instructions to be issued for FFF printers strongly depends on the level of detail of the input mesh. The language, G-code, used to drive the FFF machine is based on a very simple framework [40]. Conceptually, each node of the mesh represents a coordinate to be translated into a G-code instruction in order to deploy the outer perimeter of the physical object. Thus, the higher the number of triangles describing the surface of the model, the higher the number of instructions to be set. This could result in an extremely heavy computational effort for detailed meshes, as in medical image segmentation processing. To face the problem, many slicing software subsample

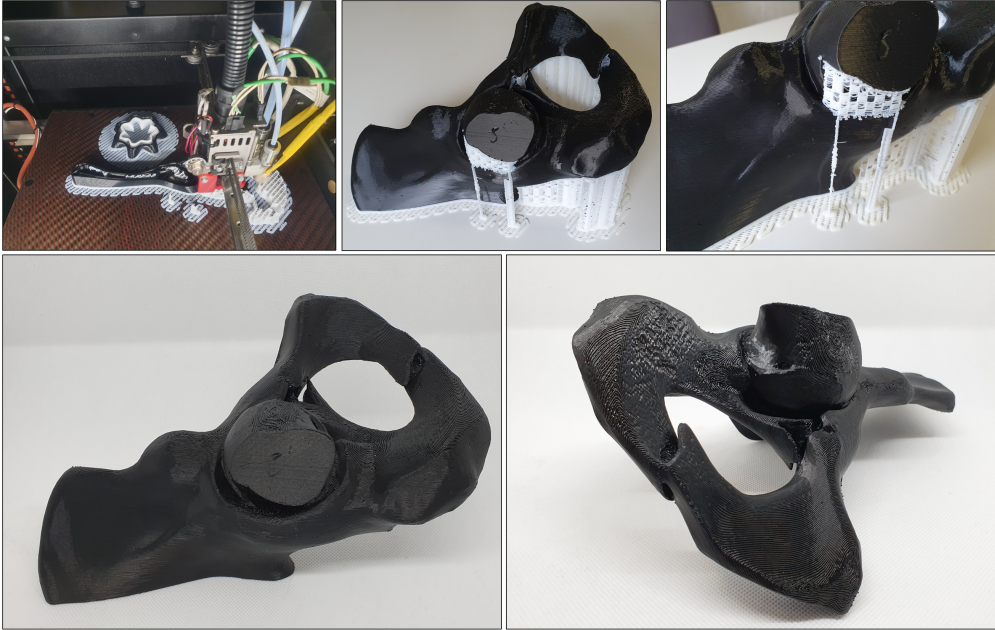


Figure 11: Validation: the 3D printed process, top-left; two views of the printed model (black: ABS) with the support material (white: HIPS), top-center and top-right; two views of the printed model after support removal, bottom.

the input geometry. In some cases, the subsample level can be tuned by the user, although in most cases this parameter cannot be controlled. In this context, the use of an adaptive mesh may be instrumental to contain the subsampling phase, since the input geometry consists of a considerable lower number of vertices.

In Figure 11, we show some pictures of the 3D printed anatomy, which is a portion of the whole anatomical district considered. We select a layer thickness of 0.3 mm, an infill of 5%, and two perimeters. The manufacturing process takes about 18 hours and further 30 minutes for the manual removal of the support structure. The features of interest, namely the fracture profiles, are correctly reproduced. As shown in Figure 11, the final 3D printed model features a detailed representation of the fracture profile, that is crucial to make the model suitable for an effective surgical planning.

7 Conclusions and perspectives

In this work, we addressed the problem of 3D image segmentation by minimizing the Ambrosio-Tortorelli functional, discretized in a finite element context. For this purpose, we devised an *optimize-then-adapt* algorithm, named MES AMIS (MESH adaptation with Alternating Minimization for Image Segmentation), that we enriched with an anisotropic mesh adaptation procedure in order to minimize the cardinality of the computational mesh for a selected accuracy on the segmentation. This allowed us to extend the approach

in [8] to the 3D case.

The results of the proposed segmentation algorithm have been compared with a reference model of a fractured human pelvis (the *ground truth* geometry) coinciding with the average of three segmentations obtained after a manual correction of the ITK-SNAP output by three expert users. This comparison has been carried out in terms of Hausdorff distance. With reference to Figure 4, it turns out that we are able to provide a segmented geometry as accurate as the *ground truth* with a 91.74% reduction of triangles.

We have also performed a thorough investigation about the robustness of the proposed algorithm to possible subsamplings of the original dataset. We have checked that we can preserve a good level of accuracy, with a contained distance variation, even when employing a small portion of the whole data. This analysis may have an impact in reducing the exposure time to the radiomagnetic waves during the MDCT scan.

In terms of computational efficiency, the current implementation of MES AMIS is not yet competitive when compared to ITK-SNAP. Indeed, while ITK-SNAP requires, on average (depending on the quality of MDCT images), a computational time of about 15-20 minutes, to move from the MDCT dataset to the final triangulated geometry, the computational time demanded by MES AMIS is on the order of hours. ITK-SNAP is very efficient thanks to the employment of a narrow band formulation. On the contrary, the current implementation of the proposed algorithm deserves to be optimized, for instance by using parallel programming. As an alternative, we can conceive to move to a level set formulation, in order to combine the accuracy of anisotropic mesh adaptation with the efficiency of the narrow band method.

Another issue that could lead to a computational improvement of MES AMIS is represented by the tuning of the parameters involved in the functional (2). In particular, we have focused on the parameters related to the tissue type, which affect the variation of the gradient of f over the image. In this work, we have limited the analysis to bone tissues only, allowing us to make a unique choice for the parameters ϵ , β and γ ($\epsilon = 10^{-3}$, $\beta = 2.0$, $\gamma = 0.1$). It is evident that the same values can not be adopted for the segmentation of tissues of different nature, e.g., soft tissues. A thorough verification in the presence of diverse datasets is consequently advisable to correctly tune the parameters involved in the MES AMIS algorithm. An automatic or semi-automatic parameter tuning remains an extremely interesting challenge.

We have also tested the effectiveness of the mesh provided by MES AMIS to create a physical replica of the pelvic bone by a FFF machine. The reduction in terms of virtual model storage brought by the adaptive approach turns out to be particularly beneficial for the generation of a contained set of the G-code instructions. In addition, the adapted mesh reduces the computational time to perform the slicing. This limits the need of subsampling the mesh, which is standard when using ITK-SNAP, and which can impair the level of detail of the model, thus preventing an effective usage for surgical planning purposes.

As a free byproduct of the adaptive approach, we emphasize that functional information from the original dataset can be directly reconstructed from the recovered image

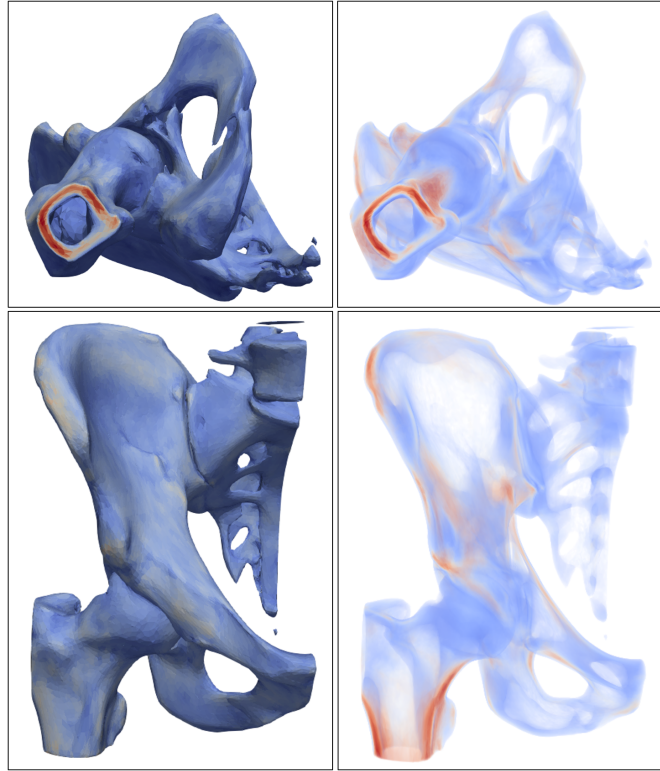


Figure 12: Views of the MES AMIS volumetric mesh including the grayscale values retrieved from the MDCT dataset. Solid views of the external surface values (left) and translucent views of the inner volume mesh elements (right).

u. As an example, it is possible to retrieve the grayscale levels of the original MDCT dataset for each element of a volumetric mesh (see Figure 12), to be used for simulation purposes or to be transformed into specific materials for AM production. With this aim, file formats like Additive Manufacturing Format (AMF) [41] or 3D Manufacturing Format (3MF) [60] have been introduced for AM purposes as an upgraded version of an STL file. Actually, these formats are based on an XML structure, and include additional information besides the geometric one, such as color or material, and property information, ready to be interpreted by most slicing software.

References

- [1] Dapogny, C., Dobrzynski, C. Frey, P.: Three-dimensional adaptive domain remeshing, implicit domain meshing, and applications to free and moving boundary problems. *J. Comput. Phys.* 262, 358–378 (2014)
- [2] Mumford, D., Shah, J.: Optimal approximations by piecewise smooth functions and associated variational problems. *Comm. Pure Appl. Math.* 42, 577–685 (1989)

- [3] De Giorgi, E., Carriero, M., Leaci, A.: Existence theorem for a minimum problem with free discontinuity set. *Arch. Ration. Mech. Anal.* 108, 195–218 (1989)
- [4] Ambrosio, L., Tortorelli, V.M.: Approximation of functionals depending on jumps by elliptic functionals via Γ -convergence. *Comm. Pure Appl. Math.* 43, 999–1036 (1990)
- [5] Ambrosio, L., Tortorelli, V.M.: On the approximation of free discontinuity problems. *Boll. Un. Mat. Ital.* 6, 105–123 (1990)
- [6] Burke, S., Ortner, C., Süli, E.: An adaptive finite element approximation of a variational model of brittle fracture. *SIAM J. Numer. Anal.* 48, 980–1012 (2010)
- [7] Artina, M., Fornasier, M., Micheletti, S., Perotto, S.: Anisotropic mesh adaptation for crack detection in brittle materials. *SIAM J. Sci. Comput.* 37, B633–B659 (2015)
- [8] Chiappa, A. S., Micheletti, S., Peli, R., Perotto, S.: Mesh adaptation-aided image segmentation. *Commun. Nonlinear Sci. Numer. Simulat.* 74, 147–166 (2019)
- [9] Caselles, V., Kimmel, R., Sapiro, G.: Geodesic active contours. *Int. J. Comput. Vision.* 22, 61–79 (1997)
- [10] Chan, T.F., Vese, L.A.: Active contours without edges. *IEEE Trans. Image Process.* 10, 266–277 (1997)
- [11] Yushkevich, P.A., Piven, J., Hazlett, H.C., Smith, R.G., Ho, S., Gee, J.C., Gerig, G.: User-guided 3D active contour segmentation of anatomical structures: significantly improved efficiency and reliability. *Neuroimage.* 31, 1116–1128 (2006)
- [12] Bourdin, B.: Image segmentation with a finite elements method. *ESAIM Math. Model. Numer. Anal.* 33, 229–244 (1999)
- [13] Zienkiewicz, C., Zhu, J.: The superconvergent patch recovery and a posteriori error estimate. Part I: The recovery technique. *Int. J. Numer. Methods Engng* 33, 1331–1364 (1992)
- [14] Zienkiewicz O.C., Zhu J.Z.: A simple error estimator and adaptive procedure for practical engineering analysis. *Int. J. Numer. Methods Engng* 24, 337–357 (1987)
- [15] Farrell, P. E., Micheletti, S., Perotto, S.: An anisotropic Zienkiewicz-Zhu-type error estimator for 3D applications. *Int. J. Numer. Methods Engng* 85, 671–692 (2011)
- [16] Farrell, P. E., Micheletti, S., Perotto, S.: A recovery-based error estimator for anisotropic mesh adaptation in CFD. *Bol. Soc. Esp. Mat. Apl.* 50, 115–138 (2010)
- [17] Formaggia, L., Perotto, S.: New anisotropic a priori error estimates. *Numer. Math.* 89, 641–667 (2001)
- [18] Frey, P., George, P.L.: *Mesh Generation: Application to Finite Elements*. Wiley-ISTE, France (2008)

- [19] Bourdin, B., Chambolle, A.: Implementation of an adaptive finite-element approximation of the Mumford-Shah functional. *Numer. Math.* 85, 609–646 (2000)
- [20] Hecht, F.: New development in FreeFem++. *J. Numer. Math.* 20, 251–265 (2012)
- [21] De Vos, W., Casselman, J., Swennen, G. R. J.: Cone-beam computerized tomography (CBCT) imaging of the oral and maxillofacial region: A systematic review of the literature. *J. Oral. Maxillofac. Surg.* 38, 609–625 (2009)
- [22] Ayachit, U.: *The ParaView Guide: A Parallel Visualization Application*. Kitware, Inc., New York, USA (2015)
- [23] Caselles, V., Kimmel, R., Sapiro, G.: Geodesic active contours. *Int. J. Comput. Vision.* 22, 61–79 (1997)
- [24] Chopp, D. L.: Computing minimal surface via level set curvature flow. *J. Comput. Phys.* 106, 77–91 (1993)
- [25] Cignoni, P., Rocchini, C., Scopigno, R.: Metro: Measuring error on simplified surfaces. *Comput. Graph. Forum.* 17, 167–174 (1998)
- [26] CloudCompare (version 2.10.2) [GPL software]. (2019). Retrieved from <http://www.cloudcompare.org/>
- [27] Yoo, T.S., Ackerman, M.J., Vannier, M.: Toward a common validation methodology for segmentation and registration algorithms. In: Delp, S.L., DiGioia, A.M., Jaramaz, B. (eds) *Medical Image Computing and Computer-Assisted Intervention – MICCAI 2000*. Lecture Notes in Computer Science, Springer 1935, 422–431 (2000)
- [28] Drechsler, K., Meixner, S., Laura, C.O., Wesarg, S.: A framework for validation of vessel segmentation algorithms. *Proceedings of the 26th IEEE International Symposium on Computer-Based Medical Systems.* 518–519 (2013)
- [29] Collins, D.L., Zijdenbos, A.P., Kollokian, V., Sled, J.G., Kabani, N.J., Holmes C.J., Evans, A.C.: Design and construction of a realistic digital brain phantom. *IEEE Trans. Med. Imaging* 17, 463–468 (1998).
- [30] Cheng, I., Sun, X., Alsufyani, N., Xiong, Z., Major, P., Basu, A.: Ground truth delineation for medical image segmentation based on Local Consistency and Distribution Map analysis. *37th Annual International Conference of the IEEE Engineering in Medicine and Biology Society (EMBC)* 3073–3076 (2015).
- [31] Warfield, S.K., Zou, K.H., Wells, W.M.: Simultaneous truth and performance level estimation (STAPLE): an algorithm for the validation of image segmentation. *IEEE Trans. Med. Imaging* 23, 903–921 (2004)

- [32] Benhabiles, H., Vandeborre, J., Lavoue, G., Daoudi, M.: A framework for the objective evaluation of segmentation algorithms using a ground-truth of human segmented 3D-models. *IEEE International Conference on Shape Modeling and Applications* 36–43 (2009)
- [33] Ballarin, M., Balletti, C., Vernier, P.: Replicas in cultural heritage: 3D printing and the museum experience. *ISPRS - International Archives of the Photogrammetry, Remote Sensing and Spatial Information Sciences. XLII-2*, 55–62 (2018)
- [34] Dietrich, C.A., Ender, A., Baumgartner, S., Mehl, A.: A validation study of reconstructed rapid prototyping models produced by two technologies. *The Angle Orthodontist* 87, 782–787 (2017)
- [35] Ender, A., Mehl, A.: Accuracy of complete-arch dental impressions: A new method of measuring trueness and precision. *The Journal of Prosthetic Dentistry* 109, 121–128 (2013)
- [36] Bortolotto, C., Eshja, E., Peroni, C., Orlandi, M., Bizzotto, N., Poggi, P.: 3D printing of CT dataset: validation of an open source and consumer-available workflow. *Journal of Digital Imaging* 109, 121–128 (2015)
- [37] Pietrabissa, A., Marconi, S., Negrello, E., Mauri, V., Peri, A., Pugliese, L., Marone, E.M., Auricchio, F.: An overview on 3D printing for abdominal surgery. *Surgical Endoscopy* 34, 1–13 (2020)
- [38] *Handbook of Medical Image Processing and Analysis*, 2nd Edition, I.N. Bankman (Ed.), Academic Press, San Diego, CA, USA, (2008)
- [39] Marconi, S., Pugliese, L., Botti, M., Peri, A., Cavazzi, E., Latteri, S., Auricchio, F., Pietrabissa, A.: Value of 3D printing for the comprehension of surgical anatomy. *Surgical Endoscopy* 31, 4102–4110 (2017)
- [40] RepRap contributors, "G-code", <https://reprap.org/mediawiki/index.php?title=G-code&oldid=187424> (accessed February 27, 2020)
- [41] Standard Specification for Additive Manufacturing File Format (AMF) Version 1.2, <https://www.astm.org/Standards/ISOASTM52915.htm> (accessed February 27, 2020)
- [42] Lorensen, W.E., Cline, H.E.: Marching cubes: a high resolution 3D surface construction algorithm. *ACM SIGGRAPH Computer Graphics* 21, 163–169 (1987)
- [43] Belhamadia, Y., Fortin, A., Bourgault, Y.: On the performance of anisotropic mesh adaptation for scroll wave turbulence dynamics in reaction-diffusion systems, *J. Comput. Appl. Math.* 271, 233–246 (2014)
- [44] Dompierre, J., Vallet, M.G., Bourgault, Y., Fortin, M., Habashi, W.G.: Anisotropic mesh adaptation: towards user-independent, mesh-independent and solver-independent CFD. Part III. Unstructured meshes, *Int. J. Numer. Methods Fluids* 39, 675–702 (2002)

- [45] Ferro, N., Micheletti, S., Perotto, S.: Anisotropic mesh adaptation for crack propagation induced by a thermal shock in 2D, *Comput. Methods Appl. Mech. Engrg.* 331, 138–158 (2018)
- [46] Formaggia, L., Micheletti, S., Perotto, S.: Anisotropic mesh adaption with application to CFD problems. *Proc. WCCM V (Fifth World Congress on Computational Mechanics, 2002)* 1481–1493.
- [47] Loseille, A., Dervieux, A., Alauzet, F.: Fully anisotropic goal-oriented mesh adaptation for 3D steady Euler equations, *J. Comput. Phys.* 229, 2866–2897 (2010)
- [48] Micheletti, S., Perotto, S., Soli, L.: Topology optimization driven by anisotropic mesh adaptation: towards a free-form design, *Comput. & Structures* 214, 60–72 (2019)
- [49] Porta, G.M., Perotto, S., Ballio, F.: Anisotropic mesh adaptation driven by a recovery-based error estimator for shallow water flow modeling, *Internat. J. Numer. Methods Fluids* 70, 269–299 (2012)
- [50] Stein, E., Ohnismus, S.: Anisotropic discretization- and model-error estimation in solid mechanics by local Neumann problems, *Comput. Methods Appl. Mech. Engrg.* 176, 363–385 (1999)
- [51] Micheletti, S., Perotto, S.: The effect of anisotropic mesh adaptation on PDE-constrained optimal control problems, *SIAM J. Control. Optim.* 49, 1793–1828 (2011)
- [52] Micheletti, S., Perotto, S.: Anisotropic mesh adaption for time-dependent problems, *Internat. J. Numer. Methods Fluids* 58, 1009–1015 (2008)
- [53] Dedè, L., Micheletti, S., Perotto, S.: Anisotropic error control for environmental applications *Appl. Numer. Math.* 58, 1320–1339 (2008)
- [54] Bourdin, B., Francfort, G.A., Marigo, J.-J.: Numerical experiments in revisited brittle fracture, *J. Mech. Phys. Solids* 48, 797–826 (2000)
- [55] Ern, A., Guermond, J.-L.: *Theory and Practice of Finite Elements*, Applied Mathematical Sciences 159, Springer-Verlag, New York, 2004
- [56] Artina, M., Fornasier, M., Micheletti, S., Perotto, S.: The benefits of anisotropic mesh adaptation for brittle fractures under plane-strain conditions, *New Challenges in Grid Generation and Adaptivity for Scientific Computing*, SEMA SIMAI Springer Ser., 5, 43–67, Perotto, S., Formaggia, L. (Eds), Springer, Cham, 2015
- [57] Artina, M., Fornasier, M., Micheletti, S., Perotto, S.: Anisotropic adaptive meshes for brittle fractures: parameter sensitivity, *Numerical Mathematics and Advanced Applications–ENUMATH 2013*, *Lect. Notes Comput. Sci. Eng.*, 103, 293–302, Abdulle, A., Deparis, S., Kressner, D., Nobile, F., Picasso, M. (Eds) Springer, Cham, 2015

- [58] Chambolle, A.: Image segmentation by variational methods: Mumford and Shah functional and the discrete approximations, *SIAM J. Appl. Math.* 55, 827–863 (1995)
- [59] D’Ambra, P., Tartaglione, G.: Solution of Ambrosio–Tortorelli model for image segmentation by generalized relaxation method, *Commun. Nonlinear Sci. Numer. Simulat.* 20, 819–831 (2015)
- [60] <https://3mf.io/specification/>

MOX Technical Reports, last issues

Dipartimento di Matematica
Politecnico di Milano, Via Bonardi 9 - 20133 Milano (Italy)

- 47/2020** Sangalli, L.M.
A novel approach to the analysis of spatial and functional data over complex domains
- 44/2020** Masci, C.; Ieva, F.; Paganoni A.M.
EM algorithm for semiparametric multinomial mixed-effects models
- 45/2020** Gatti, F.; Menafoglio, A.; Togni, N.; Bonaventura, L.; Brambilla, D.; Papini, M; Longoni, L.
A novel downscaling procedure for compositional data in the Aitchison geometry with application to soil texture data
- 46/2020** Bucelli, M.; Salvador, M.; Dede', L.; Quarteroni, A.
Multipatch Isogeometric Analysis for Electrophysiology: Simulation in a Human Heart
- 42/2020** Miglio, E.; Parolini, N.; Quarteroni, A.; Verani, M.; Zonca, S.
A spatio-temporal model with multi-city mobility for COVID-19 epidemic
- 43/2020** Quarteroni, A.; Vergara, C.
Modeling the effect of COVID-19 disease on the cardiac function: A computational study
- 41/2020** Cannistrà, M.; Masci, C.; Ieva, F.; Agasisti, T.; Paganoni, A.M.
Not the magic algorithm: modelling and early-predicting students dropout through machine learning and multilevel approach
- 40/2020** Fresca, S.; Manzoni, A.; Dedè, L.; Quarteroni, A.
Deep learning-based reduced order models in cardiac electrophysiology
- 39/2020** Martinolli, M.; Biasetti, J.; Zonca, S.; Polverelli, L.; Vergara, C.
Extended Finite Element Method for Fluid-Structure Interaction in Wave Membrane Blood Pumps
- 38/2020** Sollini, M.; Kirienco, M.; Cavinato, L.; Ricci, F.; Biroli, M.; Ieva, F.; Calderoni, L.; Tabacchi,
Methodological framework for radiomics applications in Hodgkin's lymphoma